Scilight

Materials and Sustainability

https://www.sciltp.com/journals/matsus



Article

Check for updates

Deposition-Pathway-Controlled Interfacial Chemistry and Scalability of Spatial-Atomic-Layer-Deposited Cu_2O Hole Transport Layers in Inverted Perovskite Solar Cells

Neeru Chaudhary [1,2,†], Ahmed Shahin [2,3,†], Navdeep Goyal [1] and Kevin P. Musselman [2,3,*]

[1] Department of Physics, Panjab University, Chandigarh 160014, India
[2] Department of Mechanical and Mechatronics Engineering, University of Waterloo, Waterloo, ON N2L 3G1, Canada
[3] Waterloo Institute for Nanotechnology, University of Waterloo, Waterloo, ON N2L 3G1, Canada
* Correspondence: kevin.musselman@uwaterloo.ca
† These authors contributed equally to this work.

How To Cite: Chaudhary, N.; Shahin, A.; Goyal, N.; et al. Deposition-Pathway-Controlled Interfacial Chemistry and Scalability of Spatial-Atomic-Layer-Deposited Cu_2O Hole Transport Layers in Inverted Perovskite Solar Cells. *Materials and Sustainability* **2026**, *2*(4), 8. https://doi.org/10.53941/matsus.2026.100008

Received: 10 October 2026
Revised: 10 November 2026
Accepted: 16 November 2026
Published: 23 November 2026

Abstract: Inorganic hole transport layers (HTLs) offer a promising route toward stable and scalable perovskite solar cells (PSCs), yet their performance can be limited by interfacial defects and poor control of film properties. Here, atmospheric-pressure spatial atomic layer deposition (AP-SALD) of Cu_2O is introduced as a scalable, open-air method for fabricating HTLs for inverted (p-i-n) perovskite architectures. These HTLs (SALD-Cu_2O) are systematically compared with thermally evaporated and oxidized Cu_2O HTLs (TE-Cu_2O) and poly[bis(4-phenyl) (2,4,6-trimethylphenyl) amine] (PTAA) in $FAMAPbI_3$ and $MAPbI_3$ solar cells. Perovskite crystallization is found to be better on the SALD-Cu_2O than on the TE-Cu_2O, particularly for $MAPbI_3$, resulting in larger grains and fewer pinholes. The SALD-Cu_2O HTLs are also found to have less surface hydroxylation and form less interfacial CuI than the TE-Cu_2O. Although the as-deposited power conversion efficiencies (PCE) are lower with the SALD-Cu_2O HTLs (PCE = 9.6% for $MAPbI_3$) than with the PTAA (PCE = 17.2%), the SALD-Cu_2O devices exhibit superior stability. After six months of glovebox storage, $FAMAPbI_3$ and $MAPbI_3$ cells with TE-Cu_2O and PTAA degrade completely, whereas cells with SALD-Cu_2O HTLs remain functional, with power conversion efficiencies increasing to 9.9% ($FAMAPbI_3$) and 10.8% ($MAPbI_3$), demonstrating the potential of SALD-Cu_2O as a stable inorganic HTL.

Keywords: inverted perovskite solar cells; hole transport layer; cuprous oxide; spatial atomic layer deposition; thermal evaporation; interfacial reactions

1. Introduction

The efficiency and stability of perovskite solar cells (PSCs) are greatly influenced by the design of charge transport layers (CTLs), which play a crucial role in charge extraction [1–3]. Developing and studying CTLs is of prime importance for achieving higher power conversion efficiencies and long-term operational stability. Organic CTLs such as 2,2′,7,7′-tetrakis (N, N-di-p-methoxyphenylamino)-9,9′-spirobifluorene (Spiro-OMeTAD), poly[bis(4-phenyl) (2,4,6-trimethylphenyl) amine] (PTAA), and poly(3,4-ethylenedioxythiophene) polystyrene sulfonate (PEDOT: PSS) are widely used in PSCs because of their high PCEs and ease of processability. However, these materials have high cost, limited stability, and environmental sensitivity, which are hurdles to the commercialization of perovskite solar cells. Inorganic CTLs such as CuSCN, NiO_x, and MoO_x offer better thermal and chemical stability, but achieving optimized films and interfaces is an ongoing challenge [4]. Cu_2O, with its high hole

Copyright: © 2026 by the authors. This is an open access article under the terms and conditions of the Creative Commons Attribution (CC BY) license (https://creativecommons.org/licenses/by/4.0/).
Publisher's Note: Scilight stays neutral with regard to jurisdictional claims in published maps and institutional affiliations.

mobility (10–100 cm^2/Vs), good optical transparency in the visible region, and excellent energy-level alignment with perovskites (~5.1 eV valence band maximum), has emerged as a workable inorganic hole-transport layer (HTL) [5]. In fact, numerical simulations done by Sajid et al. highlighted Cu_2O as an ideal HTL with a potential PCE of around 25.2% [6]. However, limited studies have successfully integrated Cu_2O into PSCs [7–10], and experimentally demonstrated efficiencies using Cu_2O HTLs remain lower than those achieved using organic HTLs, indicating that interface energies and defect chemistry remain critical limitations [11]. This disparity between simulations and experimentally demonstrated efficiencies may stem from practical challenges, including difficulties in fabricating uniform, pinhole-free Cu_2O HTLs with controlled thickness and the presence of defects and recombination centers at the perovskite-Cu_2O interface. For inverted planar architectures, which are promising due to their ease of fabrication and reduced hysteresis [12,13], ineffective perovskite crystallization on the Cu_2O may also be limiting photovoltaic performance.

Cu_2O HTL deposition methods studied to date include successive ionic layer adsorption and reaction, electrodeposition, spin coating, and thermal oxidation [14]. One study reported using p-type semitransparent 3-nm-thick CuO_x deposited with atmospheric-pressure spatial atomic layer deposition (AP-SALD) as a buffer layer in an n-i-p device, achieving a PCE of 20% without causing any structural damage to the underlying perovskite [15]. In the present work, Cu_2O is employed as the HTL and is synthesized using two different techniques: thermal oxidation and AP-SALD. AP-SALD is an emerging, rapid, open-air method for the scalable deposition of nanoscale layers [16–18]. In contrast to conventional atomic layer deposition (ALD) that sequentially exposes a substrate to alternating chemical precursors, AP-SALD separates the chemical precursors in space (rather than in time) and moves the substrate between the gas-phase precursor zones to build up a film, layer by layer. AP-SALD can be 1–2 orders of magnitude faster than conventional ALD and its open-air nature makes it inherently scalable (e.g., for roll-to-roll manufacturing). The thermally oxidized Cu_2O films are formed by thermal evaporation of copper followed by oxidation in open air. The AP-SALD Cu_2O (SALD-Cu_2O) and thermally evaporated and oxidized Cu_2O (TE-Cu_2O) are used as HTLs in inverted planar PSCs with formamidinium methylammonium lead iodide ($FAMAPbI_3$) and methylammonium lead iodide ($MAPbI_3$) light-absorbing layers, as shown in Figure 1a. Solar cells with PTAA as the HTL are also studied as a reference. $MAPbI_3$ and FA-rich mixed-cation $FAMAPbI_3$ were selected as light-absorbing materials to investigate the influence of the Cu_2O HTL deposition pathway across different perovskite compositions. $MAPbI_3$ serves as a widely studied benchmark absorber, while partial substitution of MA^+ with the larger FA^+ cation in $FAMAPbI_3$ modifies the effective A-site ionic radius and Goldschmidt tolerance factor, influencing the lattice structure, phase behaviour, and optoelectronic properties of the perovskite [19–21]. Comparing these two absorbers therefore allows us to evaluate whether the effects of the Cu_2O deposition route on perovskite crystallization, interfacial properties, and photovoltaic performance are consistent across different A-site compositions.

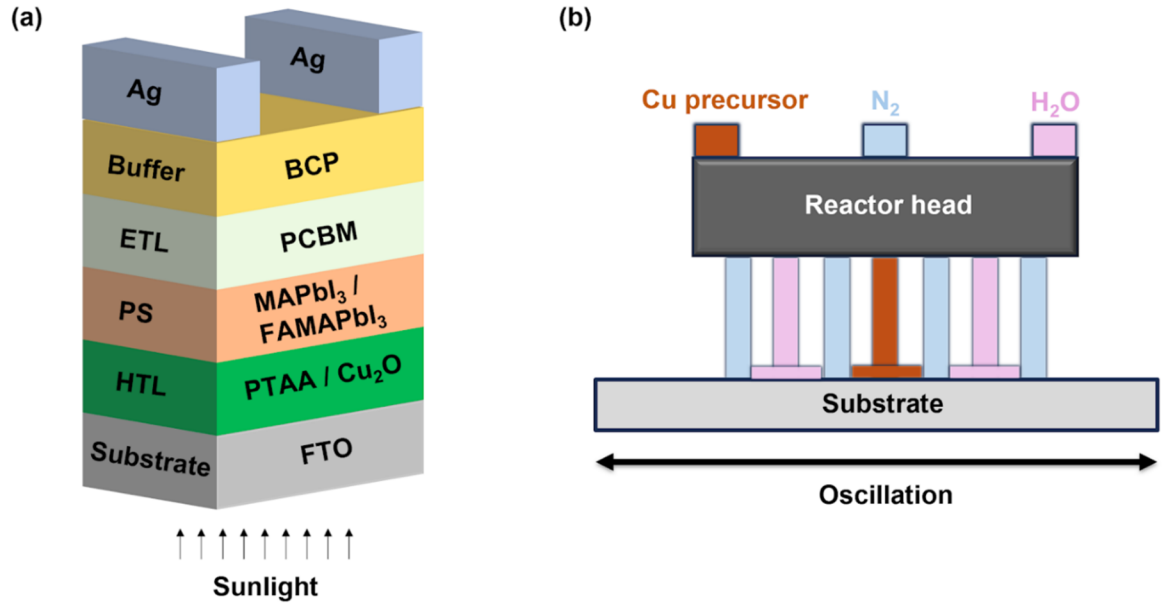

Figure 1. Experimental methodology. (**a**) Schematic of the solar cell stack, where the HTL is either PTAA, thermally evaporated and oxidized Cu_2O (TE-Cu_2O), or Cu_2O deposited by atmospheric-pressure spatial atomic layer deposition (SALD-Cu_2O), and the perovskite layer is either $FAMAPbI_3$ or $MAPbI_3$. (**b**) Schematic of SALD-Cu_2O deposition underneath an AP-SALD reactor head.

To the best of the authors' knowledge, the use of SALD-Cu_2O as a HTL in an inverted PSC has not been previously reported. By comparing Cu_2O HTLs fabricated using two different methods, this study also provides insight into the mechanistic interactions between Cu_2O and the perovskite layers. Structural and morphological analysis reveals that the type of Cu_2O HTL strongly influences the interfacial reactions and the crystallization of the perovskite layers. The SALD-Cu_2O HTL is found to perform better than the TE-Cu_2O HTL, as it enables the crystallization of a higher-quality perovskite layer; however, in as-deposited devices, the SALD-Cu_2O does not perform as well as PTAA. Composition and energy-level analysis are used to identify the cause of this deficiency. After six months of storage in the glove box, the PSCs with a SALD-Cu_2O HTL retain their photovoltaic performance, whereas PTAA and TE-Cu_2O devices exhibit complete degradation.

2. Methods

2.1. Deposition of HTLs

Fluorine-doped tin oxide (FTO)/glass substrates (16 mm × 16 mm × 2.2 mm, 7 ohm/sq, TECA7, Yingkou Shangneng Photoelectric Material Co., Ltd. (Yingkou, China)) were washed sequentially under ultrasonication in 2% ethanol, deionized water (DI) water, acetone, ethanol, and isopropanol (IPA), each for 10 min. Then the cleaned substrates were treated with UV-zone for 15 min prior to deposition of the HTL. For TE-Cu_2O, a 5-nm copper layer was deposited with a glove-box thermal evaporator (Nexdep, Angstrom Engineering) using the following deposition rates: 0 to 0.5 nm at 0.05 Å/s, 0.5–2 nm at 0.1 Å/s, and 2 to 5 nm at 0.2 Å/s, as measured using a quartz crystal microbalance. After copper deposition, the Cu_2O phase was achieved by annealing the Cu/FTO/glass on a hotplate in air at 225 °C for 15 min. SALD-Cu_2O was deposited using a custom-built, AP-SALD system reported previously [22–26]. Copper(I)/(II) Hexafluoro-2,4-Pentanedionate-Vinyltrimethylsilane ($C_{10}H_{13}CuF_6O_2Si$, commercially named CupraSelect) was used as the copper precursor. The CupraSelect was bubbled with high-purity nitrogen at a rate of 450 sccm and combined with a high-purity nitrogen carrier flow of 50 sccm. DI water was used as the oxidant. It was bubbled at 10 sccm and combined with a 490 sccm carrier nitrogen flow. The copper precursor was delivered to a single outlet channel on the bottom surface of a stainless-steel AP-SALD reactor head, as illustrated in Figure 1b. The oxidant flow was delivered to two channels. A 1500 sccm flow of nitrogen was used as gas curtains to separate the copper precursor and oxidant, as shown in Figure 1b, limiting their interaction in the gas phase and promoting their reaction as adsorbed species on the substrate surface. The FTO/glass substrates were placed on a substrate stage heated to 225 °C, which oscillated underneath the AP-SALD reactor head to sequentially expose the substrate surface to the copper precursor and oxidant. The spacing between the reactor head and the substrate was fixed at 0.1 mm. The substrate stage was oscillated 30 times to deposit SALD-Cu_2O HTLs approximately 5 nm thick, as Yu et al. reported this to be an optimum thickness for the Cu_2O [9]. The growth characteristics of the AP-SALD Cu_2O films were further evaluated by investigating the influence of Cu precursor flow rate and substrate temperature on the growth per cycle (GPC), as shown in Figure S1a,b. The GPC increased with increasing precursor flow rate before approaching saturation at 400–450 sccm. Temperature-dependent measurements revealed a relatively constant GPC between 200 and 225 °C, identifying a suitable processing window for Cu_2O-rich film growth. Spatial thickness mapping over a 35 × 35 mm^2 area further revealed a thickness distribution ranging from approximately 17.5 to 19.4 nm for a film deposited using 100 oscillations, demonstrating reasonably uniform deposition over the investigated area (Figure S1c,d). Deposition of Cu_2O via AP-SALD was confirmed via grazing-incidence X-ray diffraction (GIXRD) (Figure S2a). Photographs of the Cu_2O films prepared using the two deposition methods are provided in Figure S3 for visual comparison. Metallic Cu was selected for thermal evaporation because it enables the deposition of thin Cu layers with precise thickness control, followed by a separate oxidation step to obtain Cu_2O. In contrast, CupraSelect was selected for AP-SALD due to its sufficient volatility upon heating and compatibility with gas-phase precursor delivery. Its reaction with H_2O enables direct Cu_2O growth through sequential precursor exposure, without requiring post-deposition oxidation. For reference cells, 10 nm of PTAA (1.5–2 mg/mL in toluene) was spin-coated at 5000 rpm for 30 s and annealed at 100 °C for 10 min in a nitrogen glovebox.

2.2. Fabrication of Perovskite Solar Cells

The perovskite solar cells were fabricated in a nitrogen glovebox. To deposit the $FAMAPbI_3$ layers, 1.5 M (691.5 mg/mL) PbI_2 was dissolved in a dimethylformamide-dimethyl sulfoxide solution (DMF:DMSO, 9:1 by volume), stirred at 70 °C for 8 h, spin coated at 4000 rpm for 20 s, and then a mixed solution of FAI: MAI: MACl (90:6.39:9 mg) in IPA that was stirred for 8 h at room temperature was added to the spinning substrate for 30 s. The prepared samples were then annealed for 10 min at 110 °C. For $MAPbI_3$ layers, warm 1.2 M PbI_2 that was dissolved in DMF: DMSO (9:1) for 8 h at 70 °C was spin-coated at 2500 rpm for 20 s, and then a drop of the

mixed solution containing MAI:MACl (50:5) dissolved in IPA was added to the spinning substrate at 2500 rpm for 30 s. The prepared samples were then annealed at 70 °C for 3 min and 100 °C for 3 min. For the electron-transport layer (ETL), phenyl-C61-butyric acid methyl ester (PCBM, 20 mg/mL in chlorobenzene, dissolved for 2 h) was spin-coated at 1500 rpm for 30 s and annealed for 8 min at 100 °C. An ~8-nm interfacial layer of bathocuproine (BCP**,** 0.75 mg/mL in IPA) was spin-coated at 3000 rpm for 30 s. For the top electrodes, ~100 nm of silver (Ag) was deposited using a thermal evaporator in the glove box with the following deposition rates: 0~10 nm: 0.2~0.3 Å/s, 10~40 nm: 0.5 Å/s, 40~100 nm: 1.5 Å/s.

2.3. Characterization

Current density-voltage measurements were performed under simulated AM 1.5G solar illumination (Sciencetech UHE-NL-150 Class AAA solar simulator (Sciencetech Inc., London, ON, Canada)) in a nitrogen glovebox. The solar cell area was 0.1695 cm^2, an irradiance of 100 mW cm^{-2} was set using a NIST-traceable silicon reference solar cell, and the voltage was swept from −0.1 V to 1.2 V with a sweep rate of 0.02 V s^{-1}. For GIXRD, a PANalytical X'pert Pro MRD HR-XRD (Malvern Panalytical, Almelo, The Netherlands) was used. A VG Scientific ESCALAB**,** 250 X-ray photoelectron spectroscopy (XPS) and ultraviolet photoelectron spectroscopy (UPS) system (Thermo Fisher Scientific, East Grinstead, UK) was used to determine the composition of the Cu_2O thin films using Al Kα X-rays and the energy levels of the as-deposited films. UPS measurements were carried out using a He I photon source (21.22 eV). A –5 V sample bias was applied to accurately determine the secondary electron cutoff. The spectra were calibrated accordingly to determine the valence band maximum (VBM) and the work function. CasaXPS software (Casa Software Ltd., Teignmouth, UK) was used for processing and analysis of the spectra. Field-emission scanning electron microscopy (SEM) images were captured using a Zeiss Ultra Plus (Carl Zeiss Microscopy GmbH, Jena, Germany) in Inlense imaging mode. Grain sizes were determined from the SEM images by analyzing ~60 grains per image using Nano Measurer 1.2 software (Fudan University, Shanghai, China). Contact angle measurements were carried out to assess the surface wettability of the HTLs (PTAA, TE-Cu_2O after UV-Ozone treatment for 15 min, and SALD-Cu_2O) deposited on FTO/glass substrates. A small droplet of deionized water was drop-cast onto the surface, and images were captured using an iPhone 11 under consistent ambient lighting and fixed positioning. The contact angles were then calculated using ImageJ software (National Institutes of Health, Bethesda, MD, USA) with the Contact Angle plugin, providing a reliable estimate of the static contact angle. This method enabled straightforward evaluation of the hydrophilic or hydrophobic nature of the HTL thin films on FTO. UV-vis absorbance and photoluminescence were measured using a Horiba QuantaMaster 8000 spectrometer (HORIBA Instruments Inc., Edison, NJ, USA). The optical bandgap was determined from the UV–vis absorption using a direct-forbidden Tauc analysis by plotting $(\alpha h\nu)^{2/3}$ versus $h\nu$ and linearly extrapolating the near-edge region.

3. Results and Discussion

3.1. Photovoltaic Performance

The photovoltaic performance of the p-i-n solar cells is shown in Figure 2a,b. The short-circuit current densities (J_{sc}), open-circuit voltages (V_{oc}), fill factors (FF), and power conversion efficiencies (PCE) of the champion cells are listed in Table 1, along with the average PCEs ± standard deviation over 8 cells; champion values represent the best devices obtained in this work. For the as-fabricated $FAMAPbI_3$ (Figure 2a) and $MAPbI_3$ (Figure 2b) devices, it is seen that the reference cells with PTAA as the HTL worked the best, followed by the SALD-Cu_2O HTL, and then the TE-Cu_2O HTL. For $FAMAPbI_3$, the reference devices with PTAA had a champion PCE of 17.7% and an average PCE of 16.2 ± 0.3%, showing good reproducibility. In contrast, when TE-Cu_2O was used as the HTL, a low PCE of 4.0% was observed due to a low J_{sc} of 6.16 mA/cm^2, indicating poor charge transport. When SALD-Cu_2O was used as the HTL, the PCE improved slightly to 6.0%, limited primarily by a low V_{oc} of 0.61 V. For $MAPbI_3$, the reference devices with PTAA had a similar champion PCE of 17.2%; however, the average PCE (13.7 ± 0.7%) was lower than for $FAMAPbI_3$. The $FAMAPbI_3$ devices have generally higher J_{sc} values than the $MAPbI_3$ devices, consistent with the superior light absorption and charge transport properties of mixed cation perovskites. Again, the TE-Cu_2O HTL resulted in a low PCE (4.9%) with $MAPbI_3$ due to a low J_{sc} (8.12 mA/cm^2), indicating inefficient charge generation and/or collection. For $MAPbI_3$, the SALD-Cu_2O HTL resulted in a significantly improved device compared to the TE-Cu_2O, producing a champion PCE of 9.6% as deposited.

The performance of the devices was re-measured after storage in a nitrogen glovebox for 6 months. All devices with PTAA and TE-Cu_2O HTLs were completely degraded after the 6 months, with no measurable photovoltaic response under standard testing conditions. In contrast, the devices with SALD-Cu_2O HTLs retained their photovoltaic functionality. The champion PCE was measured to be 9.9% for the $FAMAPbI_3$ device and

10.8% for the $MAPbI_3$ device with the SALD-Cu_2O HTL. All stability measurements correspond to dark storage under a nitrogen atmosphere without encapsulation. However, the PCEs observed with the SALD-Cu_2O HTL after storage were still less than those obtained with the pristine PTAA cells. In the case of the $FAMAPbI_3$ cells, this was primarily due to a lower J_{sc} and FF (Figure 2a and Table 1). In the case of the $MAPbI_3$ cells, this was primarily due to a lower J_{sc} and V_{oc} (Figure 2b and Table 1). The reasons for the lower J_{sc} and PCE observed with the Cu_2O HTLs are investigated in the subsequent sections. The SALD-Cu_2O-based devices exhibited an increase in PCE after six months of storage under dark nitrogen conditions. The champion PCE increased from 9.6% to 10.8% for $MAPbI_3$-based devices and from 6.0% to 9.9% for $FAMAPbI_3$-based devices. For $FAMAPbI_3$, the improvement was primarily associated with an increase in V_{oc} from 0.61 to 0.93 V, whereas the $MAPbI_3$ devices exhibited an increase in FF from 62.05% to 67.88%. These improvements may be associated with gradual changes in the perovskite layers and at the Cu_2O/perovskite interfaces during storage. Possible contributing processes include structural relaxation, redistribution of mobile ionic species, and changes in interfacial defect states, which may influence charge extraction and non-radiative recombination. However, since no intermediate structural or optoelectronic characterization was performed during storage, the precise mechanisms responsible for the observed improvements cannot be established from the present results. Importantly, the devices were stored without encapsulation in the dark under a nitrogen atmosphere, without continuous illumination or electrical bias. Therefore, these measurements demonstrate shelf stability under the specified storage conditions rather than operational stability under working conditions.

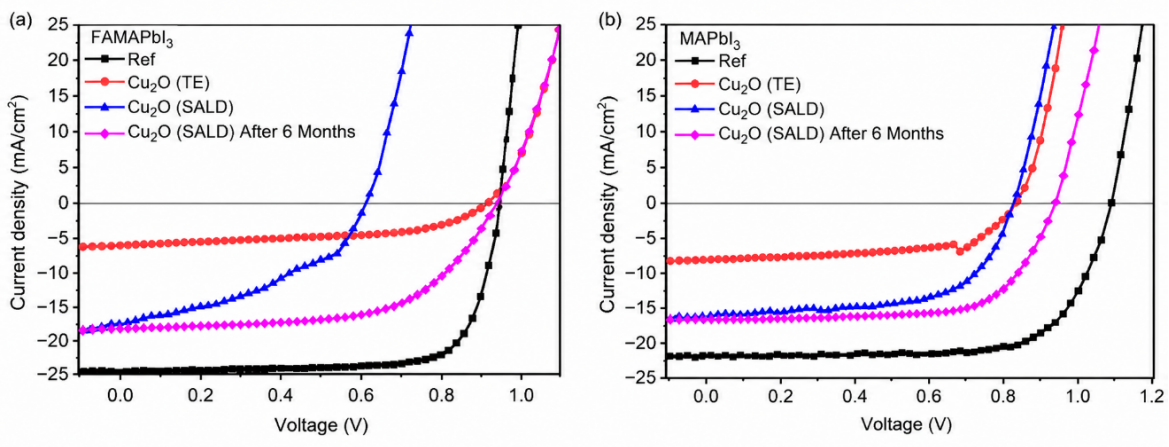

Figure 2. *J-V* measurements of (**a**) $FAMAPbI_3$ and (**b**) $MAPbI_3$ solar cells with the three different HTLs (PTAA reference, TE-Cu_2O, SALD-Cu_2O) under simulated AM 1.5G solar illumination. Measurements for SALD-Cu_2O devices after glovebox storage for 6 months are also shown. Devices with PTAA and TE-Cu_2O HTLs were completely degraded after 6 months.

Table 1. Solar cell parameters for champion cells, average PCEs (8 cells), and average perovskite grain size for different HTLs.

HTL	Perovskite	Voc (V)	Jsc (mA/cm^2)	FF	PCE (%) Champion Cell	Average PCE %	Average Grain Size (nm)
PTAA (Control)	$FAMAPbI_3$	0.95	24.90	74.95	17.7	16.2 ± 0.3	366
TE-Cu_2O		0.93	6.16	69.12	4.0	2.0 ± 0.3	344
SALD-Cu_2O		0.61	16.81	58.42	6.0	4.2 ± 0.3	357
SALD-Cu_2O (stored 6 months)		0.93	18.13	58.49	9.9	8.3 ± 0.4	-
PTAA (Control)	$MAPbI_3$	1.10	21.50	72.85	17.2	13.7 ± 0.7	296
TE-Cu_2O		0.87	8.12	69.79	4.9	2.3 ± 0.6	257
SALD-Cu_2O		0.95	16.32	62.05	9.6	8.4 ± 0.2	374
SALD-Cu_2O (stored 6 months)		0.96	16.54	67.88	10.8	9.5 ± 0.2	-

3.2. Structural Characterization of Perovskite/HTL Interfaces (GIXRD)

To understand the performance limitations of the cells using the Cu_2O HTLs, the structure of the perovskite layers deposited on the different HTLs was examined. Figure 3 shows the GIXRD patterns for the $FAMAPbI_3$ and $MAPbI_3$ films on the three HTLs. For $FAMAPbI_3$, Figure 3a confirms that the films crystallize predominantly in

the α-$FAMAPbI_3$ perovskite structure on all the HTLs with prominent peaks at 13.9°, 28.1° and 31.5° closely matching the reported JCPDS cards for $MAPbI_3$ (00-021-1276) and α-$FAPbI_3$ (00-054-1307), with slight peak shifts due to lattice expansion from mixed-cation incorporation [27–29]. A PbI_2 peak is visible in all $FAMAPbI_3$ samples at 12.65° (JCPDS 00-007-0235), indicating incomplete precursor conversion across all samples. Furthermore, an additional peak at 29.35° is visible on TE-Cu_2O, suggesting that CuI (JCPDS 00-006-0623) is formed via an interfacial reaction between Cu_2O and iodide. Similarly, Figure 3b confirms the formation of the tetragonal perovskite phase $MAPbI_3$ on all HTLs (JCPDS: 00-021-1276) with characteristic peaks at 14.1°, 28.4°, and 31.8° [30]. Again, uncompensated PbI_2 is visible in all $MAPbI_3$ samples with PbI_2 peaks at 12.65°, 25.85°, and 39.55° (JCPDS:00-007-0235). In this case, a CuI peak at 25.35° (JCPDS: 00-006-0623) is observed for both the TE-Cu_2O and SALD-Cu_2O HTLs. The observation of CuI peaks in the GIXRD analysis implies that an interfacial reaction is occurring at the HTL-perovskite interface [31]. Additional weak diffraction reflections are observed in the $FAMAPbI_3$ films deposited on PTAA and TE-Cu_2O at approximately 2θ = 11.6°, 26°, 49.6°, and 51.9°. The peaks at 11.6° and 26° are attributed to (010) and (021) reflections, respectively, from a minor hexagonal δ-$FAPbI_3$ phase [32], while the peak near 49.6° corresponds to a higher-order (222) reflection of the photoactive α-$FAPbI_3$ phase [33]. The reflection at approximately 51.9° originates from the SnO_2 component of the underlying FTO substrate [34]. These additional reflections indicate the presence of a minor secondary perovskite phase and contributions from the substrate, while the dominant diffraction peaks confirm that the films predominantly crystallize in the photoactive α-phase.

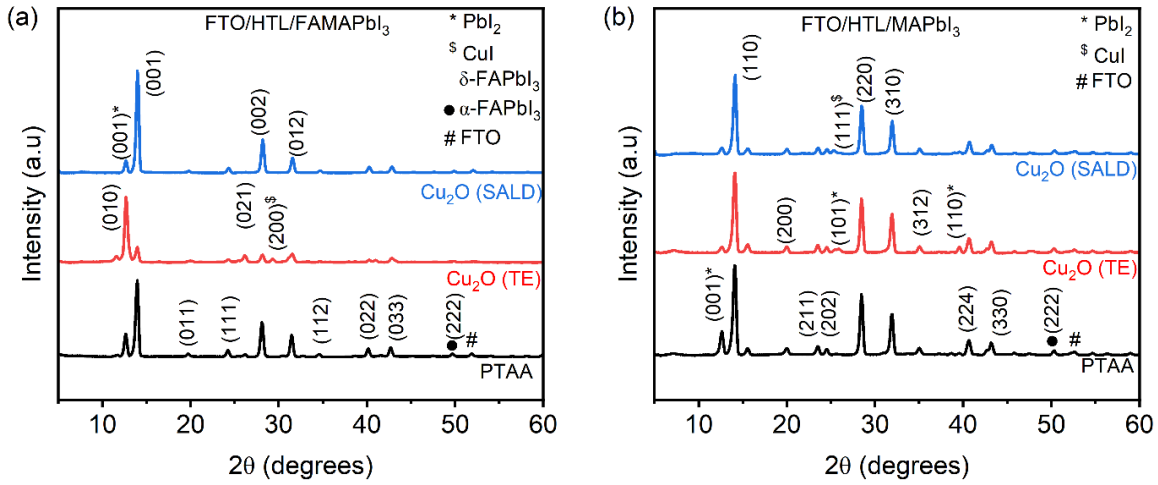

Figure 3. GIXRD patterns of (**a**) $FAMAPbI_3$ and (**b**) $MAPbI_3$ films on the three HTLs.

3.3. Chemical Composition and Oxidation State Analysis (XPS)

To assess the chemical composition and oxidation states in the Cu_2O thin films, XPS survey and high-resolution scans were performed for samples deposited by AP-SALD and TE. Figure 4a,b show the wide scan spectra, while Figure 4c–f present the core-level spectra of Cu 2p and O 1s regions. The survey spectra in Figure 4a,b confirm the presence of Cu and O as the dominant elements in both films, with negligible contamination from carbon and other elements after sputtering the films with argon for 10 s. The relative atomic percentages of O 1s, C 1s, and Cu 2p are summarized in the respective insets. The high-resolution Cu 2p spectra (Figure 3c,d) show well-defined Cu $2p_{3/2}$ and Cu $2p_{1/2}$ peaks at ~932.4 eV and ~952.2 eV, respectively, consistent with the presence of Cu^+ in Cu_2O [35]. Importantly, the absence of pronounced shake-up satellite peaks in both samples rules out significant Cu^{2+} contributions from CuO, although weak satellite features are still observed [26]. The SALD-grown film exhibits slightly sharper peaks with lower satellite intensity, which may indicate fewer surface defects or a lower degree of surface oxidation.

To further probe the oxidation states, the O 1s core-level spectra were deconvoluted (Figure 4e,f). Three major components corresponding to Cu^+ lattice oxygen (~530.5 eV), Cu^{2+} lattice oxygen (~529.7 eV), and surface hydroxyl groups (Cu–OH, ~531.4 eV) [36]. The SALD Cu_2O film shows a more prominent Cu^{2+} component compared to the TE film. However, the Cu^+ peak remains dominant in both cases, affirming Cu_2O as the primary phase. Interestingly, the relative intensity of the Cu–OH component is higher in the TE film, indicating increased surface hydroxylation. This may be attributed to post-deposition exposure to air or moisture during transfer or storage and highlights the potential benefit of inline SALD processing in limiting surface contamination and hydroxylation. Overall, XPS analysis confirms that both deposition methods produce Cu_2O-rich films with

minimal CuO content, but the SALD-grown films exhibit cleaner surfaces and a more defined Cu^+ signature. These results correlate with the better performance of the SALD-Cu_2O devices (Table 1). The more significant surface hydroxylation of the TE-Cu_2O films may inhibit charge transfer and result in recombination losses.

The prevalance of Cu^+ species at the surface of the HTLs may explain the formation of CuI. Copper electrodes, for example, have previousy been shown to react with iodide in the perovskite-precursor solution to form an interfacial CuI layer that serves as an HTL [37,38]. While CuI has been reported as an effective p-type HTL material when deliberately introduced, in the present work CuI formation is interpreted as an undesired by-product of interfacial reactions, particularly for the TE-Cu_2O. The formation of CuI could potentially disrupt the perovskite crystallization leading to unwanted phase segregation. The observation of more CuI on the TE-Cu_2O in Figure 3—at least in the case of $FAMAPbI_3$– may be attributable to a rougher TE-Cu_2O surface that would provide more Cu^+ species for CuI formation, as opposed to the smoother and conformal SALD-Cu_2O HTL (Figure S2b).

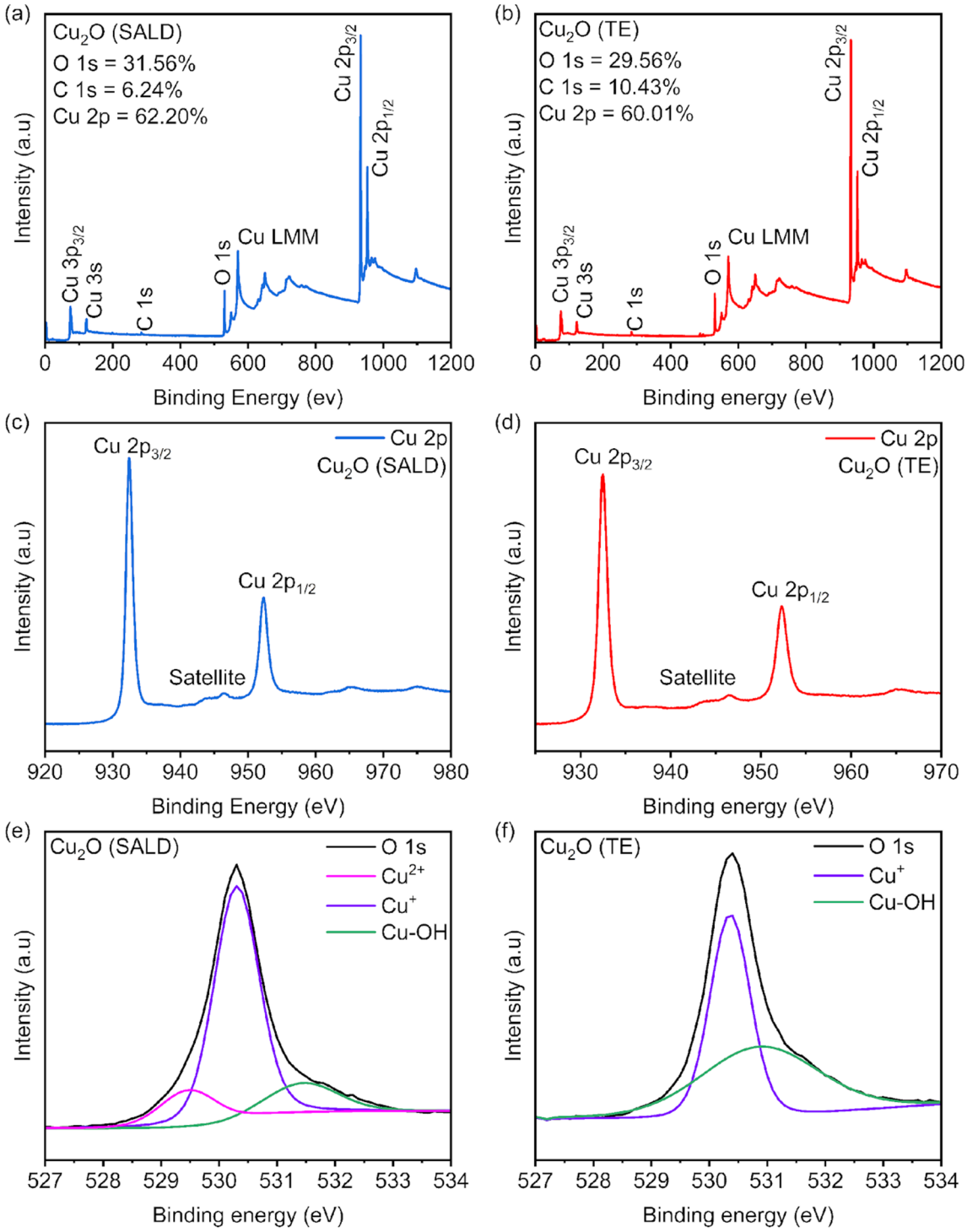

Figure 4. XPS analysis. Survey spectra of (**a**) SALD-Cu_2O and (**b**) TE-Cu_2O. Cu 2p spectra of (**c**) SALD-Cu_2O and (**d**) TE-Cu_2O. O 1s spectra of (**e**) SALD-Cu_2O and (**f**) TE-Cu_2O. All spectra were measured after 10 s of sputtering.

3.4. Effect of HTL Wettability on Perovskite Film Morphology

The morphology of the perovskite layers deposited on different HTLs was examined (Figure 5), and a strong correlation was observed with the surface wettability determined from contact angle measurements (Figure 6). For both $FAMAPbI_3$ and $MAPbI_3$, the moderate contact angle of PTAA (52.1°, Figure 6a) enables uniform wetting, resulting in largely continuous perovskite films with limited pinhole formation (Figure 5a,e). This favorable morphology is consistent with the high J_{sc}, fill factor, and PCE values observed for the PTAA-based devices (Table 1). In contrast, TE-Cu_2O exhibits a significantly larger contact angle of 123.7° (Figure 6b), indicating poor wettability, which correlates with non-uniform film coverage leading to increased pinhole density (Figure 5b,f) and, for $MAPbI_3$, a reduced grain size (Figure 5h). These morphological deficiencies are reflected in the substantially lower J_{sc}, fill factor, and PCE values obtained for TE-Cu_2O devices. The SALD-Cu_2O shows a much lower contact angle (48.3°, Figure 6c) than the TE-Cu_2O, more similar to that of the PTAA, indicating improved surface wettability. Accordingly, the perovskite films deposited on SALD-Cu_2O have grain sizes comparable to or larger than those obtained on TE-Cu_2O and PTAA (Figure 5c,d,g,h, Table 1). This larger grain size is accompanied by an enhanced J_{sc} in comparison to the TE-Cu_2O for both perovskite compositions (Figure 2). Despite this, the J_{sc} of the SALD-Cu2O-based devices remains lower than that of the PTAA-based devices, suggesting that interfacial recombination and charge transport limitations rather than bulk film morphology dominate the performance losses. Overall, the trends in device performance are consistent with the contact angle and FESEM results, highlighting the HTL wettability that governs the perovskite film formation.

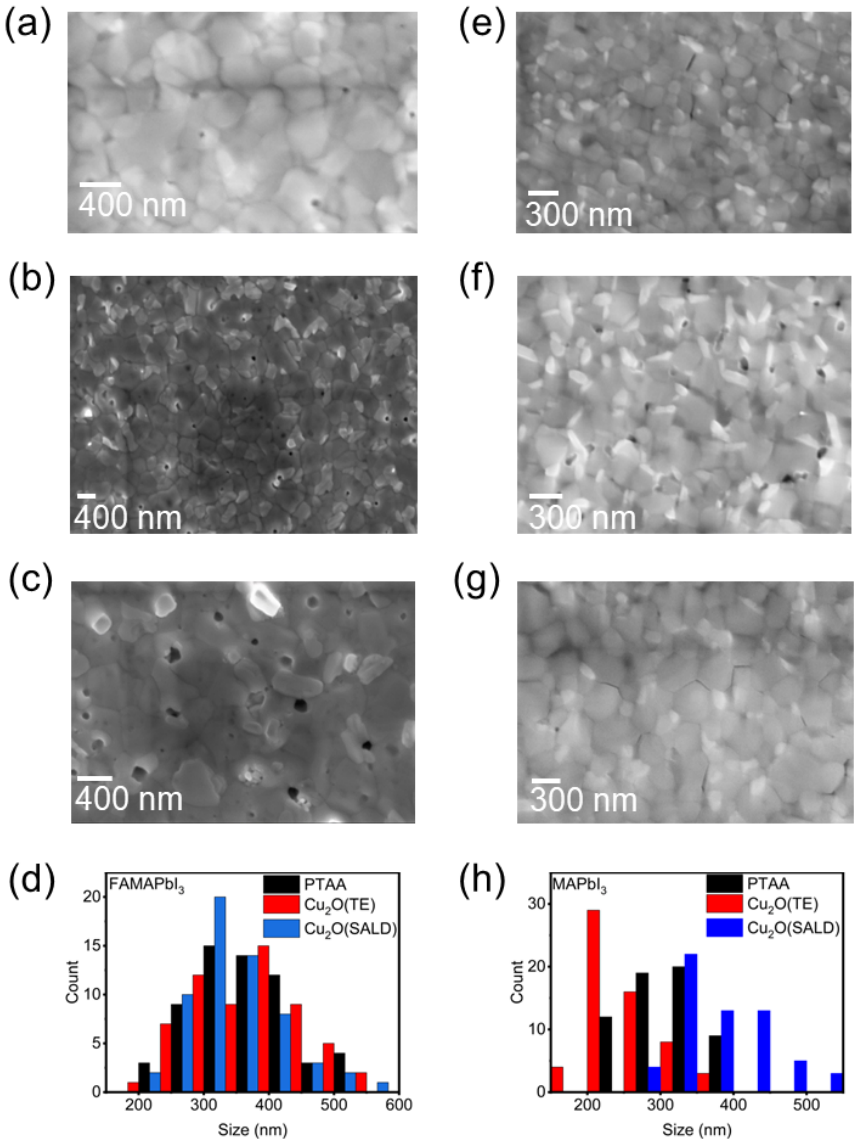

Figure 5. Morphology of perovskite layers on different HTLs. SEM images of $FAMAPbI_3$ on (**a**) PTAA; (**b**) TE-Cu_2O; and (**c**) SALD-Cu_2O. (**d**) Grain-size distribution of $FAMAPbI_3$ on the three HTLs. SEM images of $MAPbI_3$ on (**e**) PTAA; (**f**) TE-Cu_2O; and (**g**) SALD-Cu_2O. (**h**) Grain-size distribution of $MAPbI_3$ on the three HTLs.

Although SALD-Cu_2O exhibits greater water wettability than TE-Cu_2O, the resulting perovskite morphology also depends on nucleation and crystallization processes. Quantitative analysis of the SEM images in Figure 5 reveals that $FAMAPbI_3$ deposited on SALD-Cu_2O exhibits a larger average pinhole diameter (113.9 nm) and higher pinhole density (22.3 μm^{-2}) compared with TE-Cu_2O (93.75 nm and 12.8 μm^{-2}, respectively). In contrast, $MAPbI_3$ deposited on TE-Cu_2O exhibits an average pinhole diameter of 65.6 nm and a pinhole density of 33.0 μm^{-2}, whereas no discernible pinholes were detected in the $MAPbI_3$ film on SALD-Cu_2O. These findings, summarized in Table S1, suggest that the influence of the Cu_2O deposition pathway on perovskite film formation is composition-dependent, and that improved surface wettability does not necessarily eliminate pinhole formation. Such pinholes may contribute to leakage pathways and increased interfacial recombination, potentially limiting photovoltaic performance. However, the higher efficiencies obtained with SALD-Cu_2O compared with TE-Cu_2O indicate that additional factors, including interfacial chemistry and charge extraction, also govern device performance.

The significant difference in wettability between TE-Cu_2O and SALD-Cu_2O may be associated with their distinct deposition pathways, which influence the resulting surface chemistry and morphology. While TE-Cu_2O is obtained through thermal oxidation of an evaporated Cu film in air, SALD-Cu_2O is grown directly through sequential surface reactions involving the Cu precursor and H_2O oxidant. The XPS results (Figure 4e,f) reveal differences in the oxygen-related chemical states, with a greater contribution from the component assigned to surface hydroxyl groups in TE-Cu_2O. However, greater surface hydroxylation is typically associated with a more hydrophilic surface, inconsistent with the larger contact angle observed for the TE-Cu_2O. Wettability is also influenced by surface morphology and adsorbed species. As shown in Figure S4a, the TE-Cu_2O has a relatively rough surface morphology (RMS roughness of 31.7 nm on an FTO substrate with 10 nm RMS roughness), whereas SALD-Cu_2O has been shown to exhibit low nanoscale surface roughness, with an RMS roughness of 2.8 nm measured for a representative thicker film (Figure S2b). Furthermore, the XPS survey spectra (Figure S4b) reveal a higher residual carbon content in TE-Cu_2O compared with SALD-Cu_2O, even after 10 s of Ar sputtering. This difference suggests a greater contribution from residual carbonaceous species in the TE-Cu_2O sample, potentially arising from differences in processing or environmental exposure. Such species may alter the surface energy and, along with the greater surface roughness, contribute to the higher water contact angle observed for TE-Cu_2O (123.7°) compared with SALD-Cu_2O (48.3°). The contrasting wettability of the two Cu_2O films can, in turn, influence perovskite nucleation and crystallization. The resulting effects on perovskite coverage and morphology are composition-dependent, as discussed in Figure 5.

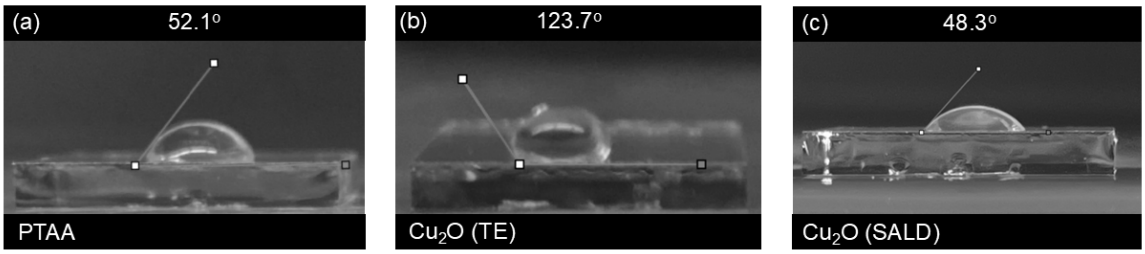

Figure 6. Contact angle measurements on different HTLs: (**a**) PTAA; (**b**) TE-Cu_2O; and (**c**) SALD-Cu_2O.

3.5. Optical Properties (UV-Vis and PL)

Next, the optical properties of the $FAMAPbI_3$ and $MAPbI_3$ layers on the different HTLs were studied. Figure 7a shows the UV-vis absorbance of the $FAMAPbI_3$ deposited on the three HTLs and an FTO/glass substrate. The absorption edge is at approximately 830 nm in all cases (near the limit of the spectrometer used) [39,40], indicating crystallization of perovskite with a band gap of approximately 1.49 eV. However, the shape of the absorption spectrum differs for the SALD-Cu_2O and particularly for the TE-Cu_2O, consistent with the pinholes observed in these films in Figure 5b,c and the PbI_2 and CuI phases detected in the GIXRD of $FAMAPbI_3$ on TE-Cu_2O (Figure 3a). The PL spectrum of the $FAMAPbI_3$ excited at 500 nm on FTO/glass in Figure 7b exhibits a single peak centered at approximately 806 nm [41], and the $FAMAPbI_3$ PL is largely quenched when placed on PTAA. No detectable PL signal is observed in Figure 7b when $FAMAPbI_3$ is crystallized on the TE-Cu_2O or SALD-Cu_2O. The low PL intensity may arise from either efficient interfacial charge transfer or unwanted non-radiative recombination due to bulk and/or interfacial defects. The low J_{sc} values for the $FAMAPbI_3$ cells on TE-Cu_2O and SALD-Cu_2O (Figure 2a) suggest that charge extraction is inhibited and hence that the low PL intensity originates from poor film quality that increases non-radiative recombination, consistent with the altered absorption spectra observed in Figure 7a.

Notably, the J_{sc} is lowest for the $FAMAPbI_3$ on TE-Cu_2O, which had the worst absorption spectrum in Figure 7a. Time-resolved PL could be performed in the future to clarify the recombination pathways.

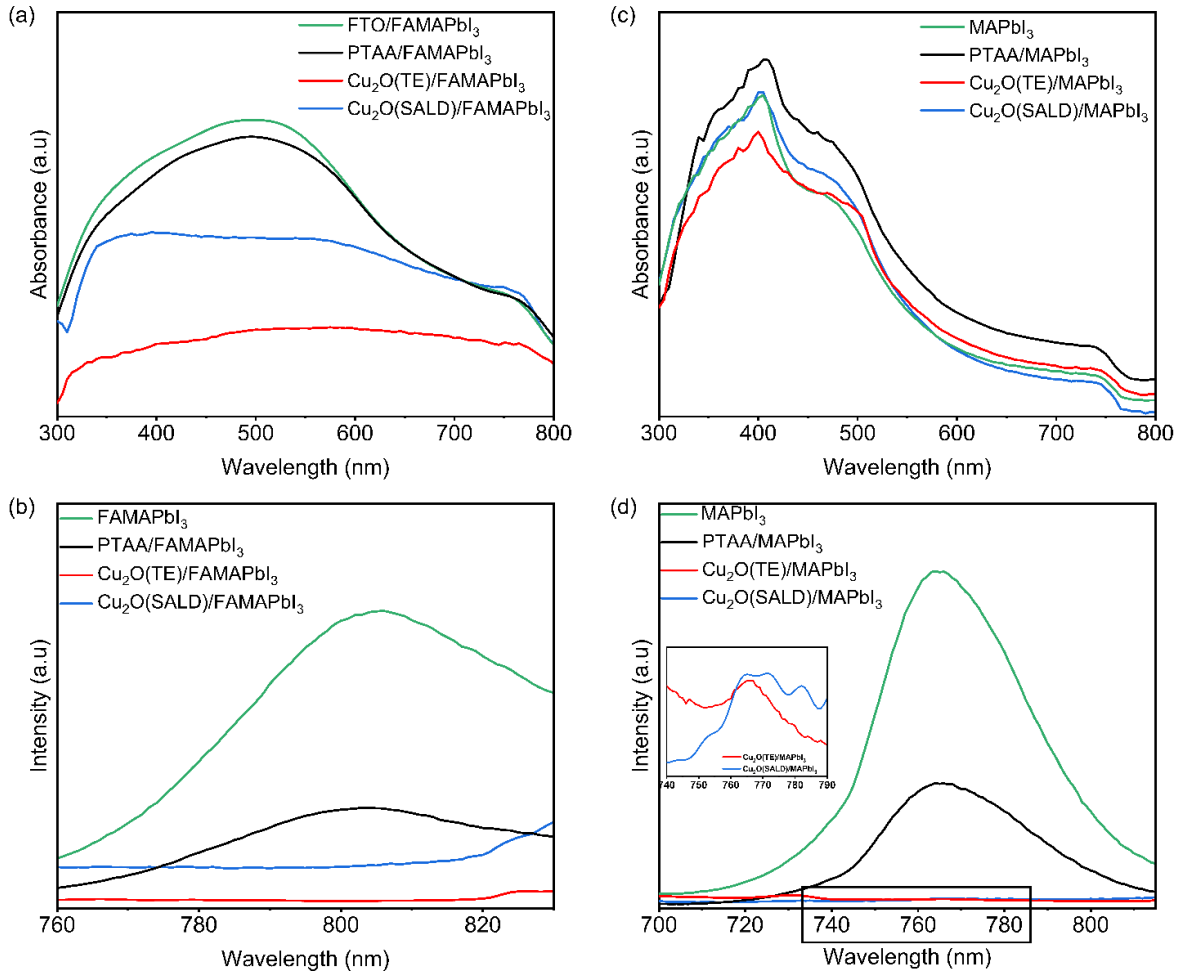

Figure 7. Optical properties of perovskite films on the three HTLs and FTO/glass. (**a**) UV-vis absorbance and (**b**) PL of $FAMAPbI_3$ films. (**c**) UV-vis absorbance and (**d**) PL of $MAPbI_3$ films.

The UV-vis absorbance of the $MAPbI_3$ and $MAPbI_3$/HTL heterostructures is shown in Figure 7c. In all cases, the absorption edge is at approximately 773 nm, corresponding to a bandgap of ~1.60 eV. In contrast to $FAMAPbI_3$, the absorption spectra of all the $MAPbI_3$ samples are similar. However, the PL spectra of the $MAPbI_3$ excited at 550 nm in Figure 7d show similar behavior to $FAMAPbI_3$: the $MAPbI_3$ on FTO/glass exhibits a strong PL peak centered at approximately 765 nm [42] that aligns well with the measured bandgap of the tetragonal $MAPbI_3$, the PTAA results in significant quenching due to hole transfer from the $MAPbI_3$, and only very weak PL peaks are observed on TE-Cu_2O and SALD-Cu_2O. The lack of PL from the $MAPbI_3$ on TE-Cu_2O is expected, given the poor perovskite morphology observed in Figure 5f and the PbI_2 and CuI phases detected by GIXRD in Figure 3b. On the other hand, the $MAPbI_3$ on SALD-Cu_2O showed a good morphology with larger grains in Figure 5g, indicating a quality perovskite layer. Hence in this case, the weak PL observed on SALD-Cu_2O in Figure 7d might be due to a combination of hole transfer from the $MAPbI_3$ to the SALD-Cu_2O (a reasonable J_{sc} of 16.32 mA/cm^2 was observed in Figure 2b) and non-radiative recombination at the $MAPbI_3$/SALD-Cu_2O interface (CuI and PbI_2 phases were observed by GIXRD in Figure 3b).

3.6. Energy-Level Alignment

To investigate the energy-level alignment within the devices, UPS was used to measure the Fermi-level offset and work function of all the Cu_2O HTLs and perovskite layers, from which the valence band maxima (VBM) were calculated (Table 2). Bandgap energies obtained from absorbance measurements and Tauc plot analysis were combined with the VBM values to identify the conduction band minima (CBM), which are also summarized in Table 2. Figure S5 provides sample UPS and UV-vis absorption data for SALD-Cu_2O, which were used to get the Fermi level offset, band gap, work

function, VBM, and CBM that are tabulated in Table 2. Based on these measurements, Figure 8 shows the energy levels of the various layers in the perovskite solar cells synthesized in this study.

Good energy-level alignment at the perovskite-HTL interface is a prerequisite for hole extraction. As shown in Figure 8, the VBM of all the HTLs, including the PTAA (−5.11 eV), TE-Cu_2O (−5.11 eV), and SALD-Cu_2O (−5.17 eV), is higher than the VBM of $FAMAPbI_3$ (−5.30 eV) and $MAPbI_3$ (−5.40 eV), which should enable efficient hole extraction from the perovskite into the HTL. Notably, SALD-Cu_2O exhibits a slightly smaller valence band offset (~0.13 eV for $FAMAPbI_3$ and ~0.23 eV for $MAPbI_3$) compared to PTAA and TE-Cu_2O (~0.19 eV for $FAMAPbI_3$ and ~0.29 eV for $MAPbI_3$); however, the device performance (Table 1) indicates that energetic alignment alone does not govern device performance. Instead, the superior efficiencies of the PTAA-based devices (17.2–17.7%), can be attributed to the better interfaces formed with the perovskite layer.

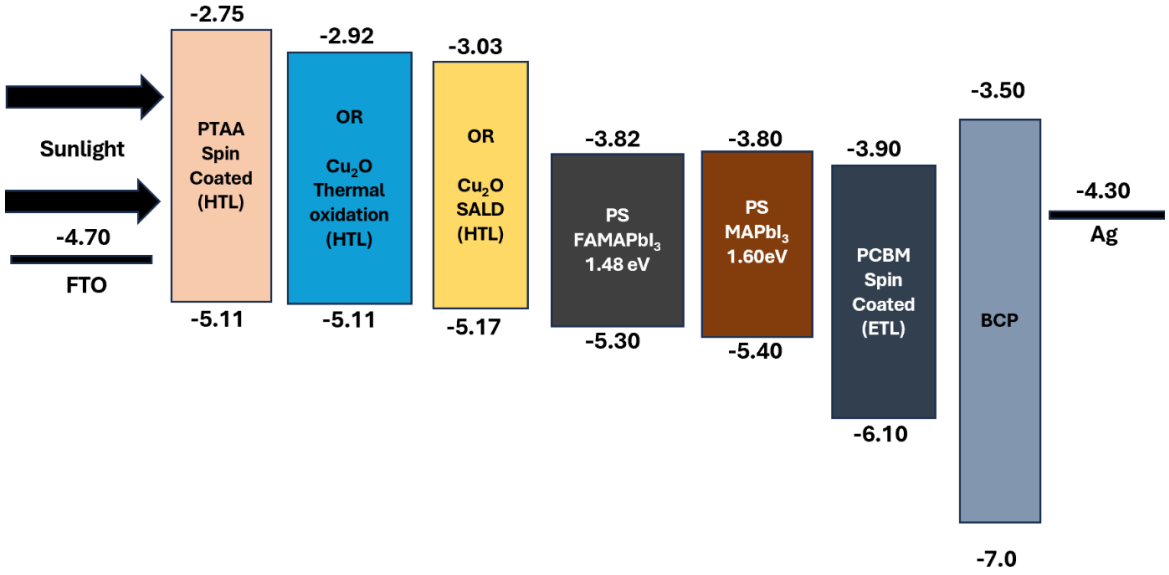

Figure 8. Energy-level of alignment of the solar cells, based on UPS and absorbance measurements of the HTL and perovskite layers.

Table 2. Energy levels of the perovskite and Cu_2O-based HTLs.

Sample	Fermi Level Offset (eV)	Work Function (eV)	VBM (eV)	Band Gap (eV)	CBM (eV)
$FAMAPbI_3$	1.07	4.23	−5.30	1.48	−3.82
$MAPbI_3$	1.05	4.35	−5.40	1.60	−3.80
TE-Cu_2O	0.34	4.77	−5.11	2.19	−2.92
SALD-Cu_2O	0.15	5.02	−5.17	2.14	−3.03

All energy levels are referenced to the vacuum level.

4. Conclusions

This work demonstrated atmospheric-pressure spatial atomic layer deposition of Cu_2O as a hole transport layer in $FAMAPbI_3$ and $MAPbI_3$ inverted perovskite solar cells. As-deposited, devices incorporating SALD-Cu_2O HTLs were more efficient than those with thermally evaporated and oxidized Cu_2O HTLs, which was attributed to a superior interface and improved perovskite crystallization. Less CuI formation and less surface hydroxylation were observed for the SALD-Cu_2O HTLs than for the TE-Cu_2O HTLs. The TE-Cu_2O was found to have poor wettability (water contact angle of 123.7°), which resulted in pinholes in both the $FAMAPbI_3$ and $MAPbI_3$ films, as well as a reduced $MAPbI_3$ grain size. In contrast, the SALD-Cu_2O showed wettability (water contact angle of 48.3°) similar to that of a reference PTAA HTL, which resulted in fewer pinholes and larger grains, particularly for $MAPbI_3$ films. The as-deposited devices with SALD-Cu_2O HTLs, however, were not as efficient as reference devices with PTAA HTLs. Weak PL signals for the $FAMAPbI_3$ and $MAPbI_3$ films on the Cu_2O HTLs suggested significant non-radiative recombination at the Cu_2O-perovskite interfaces, which may be attributable to unwanted CuI and PbI_2 phases observed by GIXRD. Time-resolved PL studies may be pursued in the future to resolve the charge-transfer and recombination pathways.

Although the initial power conversion efficiencies were lower on SALD-Cu_2O than on PTAA, the solar cells with SALD-Cu_2O HTLs demonstrated improved long-term device stability.

The $FAMAPbI_3$ and $MAPbI_3$ cells using PTAA and TE-Cu_2O degraded after 6 months of storage in a nitrogen glovebox, whereas the cells with SALD-Cu_2O retained their photovoltaic functionality, with post-storage champion PCEs of 9.9% and 10.8%. These results highlight the potential of SALD-Cu_2O as a hole transport layer for enhancing the storage stability of inverted perovskite solar cells. Nevertheless, further investigations under continuous illumination and operating conditions are required to establish the operational stability of these devices.

Together, these results highlight the potential of SALD-Cu_2O as a low-cost and durable inorganic HTL for inverted perovskite solar cells. Further optimization of interfacial passivation and controlled doping could bridge the efficiency gap with organic HTLs and enable stable, industrially viable perovskite photovoltaics.

Supplementary Materials

The additional data and information can be downloaded at: https://media.sciltp.com/articles/others/261123 1123500044/MatSus-26100065-SM.pdf. Figure S1. Growth characteristics and spatial uniformity of AP-SALD Cu_2O films. Growth per cycle (GPC) as a function of (a) Cu precursor flow rate and (b) deposition temperature. Error bars represent spatial variations in film thickness. (c) Photograph of a deposited Cu_2O film and (d) corresponding thickness map over a 35 × 35 mm^2 area. Figure S2. Confirmation of conformal Cu_2O deposition via AP-SALD. (a) GIXRD measurement showing (111) and (200) characteristic reflections of Cu_2O. (b) AFM scan of Cu_2O, deposited on ITO. The Cu_2O film on ITO had a root mean square surface roughness of 2.8 nm. The Cu_2O films for this analysis were approximately 40 nm thick. Figure S3. Photograph of Cu_2O thin films prepared by atmospheric-pressure spatial atomic layer deposition (SALD-Cu_2O, left) and thermal evaporation followed by oxidation (TE-Cu_2O, right). Figure S4. (a) 3D AFM image of TE-Cu_2O showing an RMS roughness of 31.7 nm on FTO/glass. (b) XPS C 1s spectra of TE-Cu_2O and SALD-Cu_2O, showing a higher carbon signal for TE-Cu_2O (10 s of Ar sputtering). Figure S5. Optical and electronic structure of SALD-Cu_2O thin films. (a) UV–vis absorption spectrum of SALD-Cu_2O. (b) Direct-forbidden transition Tauc analysis $(\alpha h\nu)^{2/3}$ vs $h\nu$, yielding an optical bandgap of 2.14 eV from the linear extrapolation to $(\alpha h\nu)^{2/3} = 0$. (c) Ultraviolet photoelectron spectroscopy (UPS, He I, $h\nu = 21.22$ eV) showing the secondary electron cutoff and valence-band edge offset from the Fermi level used to determine the work function and valence band maximum relative to vacuum; the conduction band minimum is then obtained using the measured bandgap. Table S1. Comparison of average pinhole size and density in $FAMAPbI_3$ and $MAPbI_3$ films deposited on thermally evaporated and oxidized Cu_2O (TE-Cu_2O) and spatial-ALD-deposited Cu_2O (SALD-Cu_2O), determined from SEM image analysis.

Author Contributions

N.C.: conceptualization, methodology, experimental investigation, data curation, original draft; A.S.: methodology, experimental investigation, formal analysis, writing review & editing; N.G.: supervision, resources, writing review & editing; K.P.M.: conceptualization, supervision, resources, project administration, funding, acquisition, writing review & editing. All authors have read and agreed to the published version of the manuscript.

Funding

This research was funded by NSERC [RTI-2021-00068, RGPIN-03548-2023], the Canada Foundation for Innovation (CFI) [John R. Evans Leaders Fund Project 41595], and the Ontario Research Fund—Research Infrastructure [Project 41595].

Institutional Review Board Statement

Not applicable.

Informed Consent Statement

Not applicable.

Data Availability Statement

The datasets generated or analyzed during the current study are available from the corresponding author on reasonable request.

Acknowledgments

N.C. acknowledges Panjab University, Chandigarh, India, for granting study leave to conduct this research. A.S. acknowledges support from an NSERC Vanier Canada Graduate Scholarship [CGV–198799]. K.P.M. acknowledges a Waterloo Endowed Chair in Nanotechnology. The authors thank the Department of Mechanical and Mechatronics Engineering at the University of Waterloo and K.P.M.'s group for access to research facilities, resources, and technical support that facilitated the research. The authors also acknowledge M.H. Azar for helpful discussions.

Conflicts of Interest

Given the role as an Editorial Board Member, K.P.M. had no involvement in the peer review of this paper and had no access to information regarding its peer-review process. Full responsibility for the editorial process of this paper was delegated to another editor of the journal.

Use of AI and AI-Assisted Technologies

No AI tools were utilized for this paper.

References

1. Noman, M.; Khan, Z.; Jan, S.T. A Comprehensive Review on the Advancements and Challenges in Perovskite Solar Cell Technology. *RSC Adv.* **2024**, *14*, 5085–5131. https://doi.org/10.1039/d3ra07518d.
2. Zhang, P.P.; Zhou, Z.J.; Kou, D.X.; et al. Perovskite Thin Film Solar Cells Based on Inorganic Hole Conducting Materials. *Int. J. Photoenergy* **2017**, *2017*, 6109092. https://doi.org/10.1155/2017/6109092.
3. Mahajan, P.; Padha, B.; Verma, S.; et al. Review of Current Progress in Hole-Transporting Materials for Perovskite Solar Cells. *J. Energy Chem.* **2022**, *68*, 330–386. https://doi.org/10.1016/j.jechem.2021.12.003.
4. Kim, M.; Kim, J. Recent Research Trends in Inorganic Charge Transport Materials for Next-Generation Perovskite Solar Cells. *Renew. Sustain. Energy Rev.* **2025**, *219*, 115835. https://doi.org/10.1016/j.rser.2025.115835.
5. Chatterjee, S.; Pal, A.J. Introducing Cu_2O Thin Films as a Hole-Transport Layer in Efficient Planar Perovskite Solar Cell Structures. *J. Phys. Chem. C* **2016**, *120*, 1428–1437. https://doi.org/10.1021/acs.jpcc.5b11540.
6. Sajid, S.; Alzahmi, S.; Ben Salem, I.; et al. Perovskite-Surface-Confined Grain Growth for High-Performance Perovskite Solar Cells. *Nanomaterials* **2022**, *12*, 3352. https://doi.org/10.3390/nano12193352.
7. Lin, L.; Jiang, L.; Li, P.; et al. A Modeled Perovskite Solar Cell Structure with a Cu_2O Hole-Transporting Layer Enabling over 20% Efficiency by Low-Cost Low-Temperature Processing. *J. Phys. Chem. Solids* **2019**, *124*, 205–211. https://doi.org/10.1016/j.jpcs.2018.09.024.
8. Chen, Y.J.; Li, M.H.; Huang, J.C.A.; et al. Cu/Cu_2O Nanocomposite Films as a p-Type Modified Layer for Efficient Perovskite Solar Cells. *Sci. Rep.* **2018**, *8*, 7646. https://doi.org/10.1038/s41598-018-25975-8.
9. Yu, W.; Li, F.; Wang, H.; et al. Ultrathin Cu_2O as an Efficient Inorganic Hole Transporting Material for Perovskite Solar Cells. *Nanoscale* **2016**, *8*, 6173–6179. https://doi.org/10.1039/c5nr07758c.
10. Liu, L.; Xi, Q.; Gao, G.; et al. Cu_2O Particles Mediated Growth of Perovskite for High Efficient Hole-Transporting-Layer Free Solar Cells in Ambient Conditions. *Sol. Energy Mater. Sol. Cells* **2016**, *157*, 937–942. https://doi.org/10.1016/j.solmat.2016.08.013.
11. Moone, P.K.; Sharifi, N. Performance and Stability of Different All-Inorganic and Hybrid Organic-Inorganic Perovskites in P-N Planar Device Structure FTO/SnO_2/Perovskite/Cu_2O/Carbon Using SCAPS-1D Simulation. *J. Opt.* **2026**, *55*, 1060–1075. https://doi.org/10.1007/s12596-024-02168-3.
12. Yang, J.; Luo, X.; Zhou, Y.; et al. Recent Advances in Inverted Perovskite Solar Cells: Designing and Fabrication. *Int. J. Mol. Sci.* **2022**, *23*, 11792. https://doi.org/10.3390/ijms231911792.
13. Lemercier, T.; Perrin, L.; Berson, S.; et al. Innovative PIN-Type Perovskite Solar Cells with 17% Efficiency: Processing and Characterization. *Mater. Adv.* **2021**, *2*, 7907–7921. https://doi.org/10.1039/d1ma00819f.
14. Chuang, T.H.; Chen, Y.H.; Sakalley, S.; et al. Highly Stable and Enhanced Performance of p–i–n Perovskite Solar Cells via Cuprous Oxide Hole-Transport Layers. *Nanomaterials* **2023**, *13*, 1363. https://doi.org/10.3390/nano13081363.
15. Jagt, R.A.; Huq, T.N.; Hill, S.A.; et al. Rapid Vapor-Phase Deposition of High-Mobility *P*-Type Buffer Layers on Perovskite Photovoltaics for Efficient Semitransparent Devices. *ACS Energy Lett.* **2020**, *5*, 2456–2465. https://doi.org/10.1021/acsenergylett.0c00763.
16. Hoye, R.L.Z.; Muñoz-Rojas, D.; Sun, Z.; et al. Spatial Atomic Layer Deposition for Energy and Electronic Devices. *PRX Energy* **2025**, *4*, 017002. https://doi.org/10.1103/prxenergy.4.017002.

17. Musselman, K.P.; Uzoma, C.F.; Miller, M.S. Nanomanufacturing: High-Throughput, Cost-Effective Deposition of Atomic Scale Thin Films via Atmospheric Pressure Spatial Atomic Layer Deposition. *Chem. Mater.* **2016**, *28*, 8443–8452. https://doi.org/10.1021/acs.chemmater.6b03077.
18. Shahin, A.; Saini, A.; Vidish, D.; et al. Scalable Single-Step Open-Air Combinatorial Growth of Multifunctional Metal Oxide Thin Films by Spatial Atomic Layer Deposition. *ACS Appl. Mater. Interfaces* **2026**, *18*, 48449–48463. https://doi.org/10.1021/acsami.6c12174.
19. Weber, O.J.; Charles, B.; Weller, M.T. Phase Behaviour and Composition in the Formamidinium–Methylammonium Hybrid Lead Iodide Perovskite Solid Solution. *J. Mater. Chem. A* **2016**, *4*, 15375–15382. https://doi.org/10.1039/c6ta06607k.
20. Kieslich, G.; Sun, S.; Cheetham, A.K. An Extended Tolerance Factor Approach for Organic–Inorganic Perovskites. *Chem. Sci.* **2015**, *6*, 3430–3433. https://doi.org/10.1039/c5sc00961h.
21. Eperon, G.E.; Beck, C.E.; Snaith, H.J. Cation Exchange for Thin Film Lead Iodide Perovskite Interconversion. *Mater. Horizons* **2016**, *3*, 63–71. https://doi.org/10.1039/c5mh00170f.
22. Durgamahanti, P.; Kharsah, O.; Zhang, J.; et al. Rapid Nucleation of ZnO on MoS_2 and WS_2 Using an Atmospheric-Pressure Spatial Atomic Layer Deposition System. *2D Mater.* **2025**, *12*, 035011. https://doi.org/10.1088/2053-1583/adda02.
23. Asgarimoghaddam, H.; Chen, Q.; Ye, F.; et al. Zinc Aluminum Oxide Encapsulation Layers for Perovskite Solar Cells Deposited Using Spatial Atomic Layer Deposition. *Small Methods* **2024**, *8*, 2300995. https://doi.org/10.1002/smtd.202300995.
24. Yeow, T.W.K.; Mistry, K.; Shahin, A.; et al. Atmospheric-Pressure Spatial Chemical Vapor Deposition of Tungsten Oxide. *J. Vac. Sci. Technol. A* **2020**, *38*, 052411. https://doi.org/10.1116/6.0000347.
25. Asgarimoghaddam, H.; Chen, Q.; Ye, F.; et al. Spatial Atomic Layer Deposition of Nitrogen-Doped Alumina Thin Films for High-Performance Perovskite Solar Cell Encapsulation. *Nano Energy* **2024**, *127*, 109782. https://doi.org/10.1016/j.nanoen.2024.109782.
26. Shahin, A.; Saini, A.; Kim, N.Y.; et al. Tailoring CuO_xFilms via Open-Air Spatial Atomic Layer Deposition and Their Application in Room-Temperature Humidity Sensing. *Small* **2025**, *21*, e06835. https://doi.org/10.1002/smll.202506835.
27. Targhi, F.F.; Jalili, Y.S.; Kanjouri, F. $MAPbI_3$ and $FAPbI_3$ Perovskites as Solar Cells: Case Study on Structural, Electrical and Optical Properties. *Results Phys.* **2018**, *10*, 616–627. https://doi.org/10.1016/j.rinp.2018.07.007.
28. Murugadoss, G.; Arunachalam, P.; Panda, S.K.; et al. Crystal Stabilization of α-$FAPbI_3$ Perovskite by Rapid Annealing Method in Industrial Scale. *J. Mater. Res. Technol.* **2021**, *12*, 1924–1930. https://doi.org/10.1016/j.jmrt.2021.03.107.
29. Chang, K.C.; Yeh, T.H.; Lee, H.Y.; et al. High Performance Perovskite Solar Cells Using Multiple Hole Transport Layer and Modulated $FA_xMA_{1-x}PbI_3$ Active Layer. *J. Mater. Sci. Mater. Electron.* **2020**, *31*, 4135–4141. https://doi.org/10.1007/s10854-020-02961-3.
30. Fan, P.; Gu, D.; Liang, G.X.; et al. High-Performance Perovskite $CH_3NH_3PbI_3$ Thin Films for Solar Cells Prepared by Single-Source Physical Vapour Deposition. *Sci. Rep.* **2016**, *6*, 29910. https://doi.org/10.1038/srep29910.
31. Gong, C.H.; Li, Z.Y.; Chen, K.W.; et al. Synthesis and Characterization of Cu_2O@Cu/Al-CLDH for Efficient Adsorption of Iodide Anions in Aqueous Solutions. *J. Radioanal. Nucl. Chem.* **2023**, *332*, 2793–2805. https://doi.org/10.1007/s10967-023-08943-z.
32. Zhang, M.; Zhang, F.; Wang, Y.; et al. High-Performance Photodiode-Type Photodetectors Based on Polycrystalline Formamidinium Lead Iodide Perovskite Thin Films. *Sci. Rep.* **2018**, *8*, 11157. https://doi.org/10.1038/s41598-018-29147-6.
33. Jin, R.-J.; Lou, Y.-H.; Huang, L.; et al. Photochemical Shield Enabling Highly Efficient Perovskite Photovoltaics. *Adv. Mater.* **2024**, *36*, 2313154. https://doi.org/10.1002/adma.202313154.
34. Miró-Zárate, J.L.; Elías-Espinosa, M.C.; Cervantes-Sodi, F.; et al. Effects of NH_4SCN Additive in the $FAPbI_3$ Perovskite Films in a Sequential Deposition Method. *Crystals* **2023**, *13*, 795. https://doi.org/10.3390/cryst13050795.
35. Biesinger, M.C. Advanced Analysis of Copper X-ray Photoelectron Spectra. *Surf. Interface Anal.* **2017**, *49*, 1325–1334. https://doi.org/10.1002/sia.6239.
36. Kalita, N.; Nath, U.; Singha, A.; et al. Electronic Structure Tuning to Facilitate Charge Transfer in Z-Scheme Mediated CuO/Se@WO_3 Aided by Synchronized $Cu(OH)_2$ for Efficient Overall Water Splitting. *J. Mater. Chem. A* **2025**, *13*, 10723–10735. https://doi.org/10.1039/d5ta00627a.
37. Nazari, P.; Ansari, F.; Abdollahi Nejand, B.; et al. Physicochemical Interface Engineering of CuI/Cu as Advanced Potential Hole-Transporting Materials/Metal Contact Couples in Hysteresis-Free Ultralow-Cost and Large-Area Perovskite Solar Cells. *J. Phys. Chem. C* **2017**, *121*, 21935–21944. https://doi.org/10.1021/acs.jpcc.7b07061.
38. Udalova, N.N.; Nemygina, E.M.; Zharenova, E.A.; et al. New Aspects of Copper Electrode Metamorphosis in Perovskite Solar Cells. *J. Phys. Chem. C* **2020**, *124*, 24601–24607. https://doi.org/10.1021/acs.jpcc.0c06608.
39. Senno, M.; Tinte, S. Mixed Formamidinium–Methylammonium Lead Iodide Perovskite from First-Principles: Hydrogen-Bonding Impact on the Electronic Properties. *Phys. Chem. Chem. Phys.* **2021**, *23*, 7376–7385. https://doi.org/10.1039/d0cp06713j.

40. Alsalloum, A.Y.; Turedi, B.; Almasabi, K.; et al. 22.8%-Efficient Single-Crystal Mixed-Cation Inverted Perovskite Solar Cells with a near-Optimal Bandgap. *Energy Environ. Sci.* **2021**, *14*, 2263–2268. https://doi.org/10.1039/d0ee03839c.
41. Slimi, B.; Mollar, M.; Ben Assaker, I.; et al. Perovskite $FA_{1-x}MA_xPbI_3$ for Solar Cells: Films Formation and Properties. *Energy Procedia* **2016**, *102*, 87–95. https://doi.org/10.1016/j.egypro.2016.11.322.
42. Stolterfoht, M.; Caprioglio, P.; Wolff, C.M.; et al. The Impact of Energy Alignment and Interfacial Recombination on the Internal and External Open-Circuit Voltage of Perovskite Solar Cells. *Energy Environ. Sci.* **2019**, *12*, 2778–2788. https://doi.org/10.1039/c9ee02020a